# High Power Factor and Enhanced Thermoelectric Performance of SnTe-AgInTe$_2$: Synergistic Effect of Resonance Level and Valence Band Convergence

Ananya Banik,[†] U. Sandhya Shenoy,[§] Sujoy Saha,[†] Umesh V. Waghmare,[§] and Kanishka Biswas[*,†]

[†]New Chemistry Unit and [§]Theoretical Sciences Unit, Jawaharlal Nehru Centre for Advanced Scientific Research (JNCASR), Jakkur P.O., Bangalore 560064, India

Ⓢ Supporting Information

ABSTRACT: Understanding the basis of electronic transport and developing ideas to improve thermoelectric power factor are essential for production of efficient thermoelectric materials. Here, we report a significantly large thermoelectric power factor of ~31.4 μW/cm·K^2 at 856 K in Ag and In co-doped SnTe (i.e., SnAg$_x$In$_x$Te$_{1+2x}$). This is the highest power factor so far reported for SnTe-based material, which arises from the synergistic effects of Ag and In on the electronic structure and the improved electrical transport properties of SnTe. In and Ag play different but complementary roles in modifying the valence band structure of SnTe. In-doping introduces resonance levels inside the valence bands, leading to a significant improvement in the Seebeck coefficient at room temperature. On the other hand, Ag-doping reduces the energy separation between light- and heavy-hole valence bands by widening the principal band gap, which also results in an improved Seebeck coefficient. Additionally, Ag-doping in SnTe enhances the p-type carrier mobility. Co-doping of In and Ag in SnTe yields synergistically enhanced Seebeck coefficient and power factor over a broad temperature range because of the synergy of the introduction of resonance states and convergence of valence bands, which have been confirmed by first-principles density functional theory-based electronic structure calculations. As a consequence, we have achieved an improved thermoelectric figure of merit, $zT \approx 1$, in SnAg$_{0.025}$In$_{0.025}$Te$_{1.05}$ at 856 K.
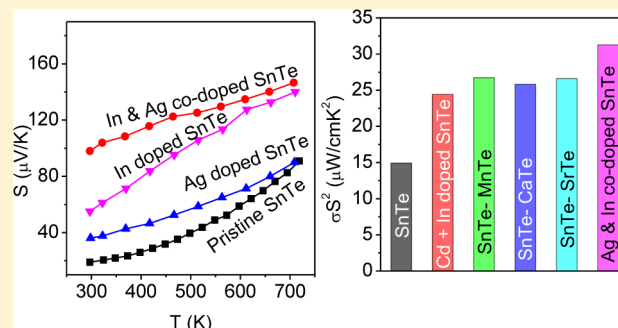
■ INTRODUCTION

Thermoelectric materials have received attention worldwide, as they can convert waste heat to electricity.[1] The efficiency of a thermoelectric material is governed by the material's figure of merit, $zT = \sigma S^2 T/\kappa_{total}$, where σ is electrical conductivity, S is Seebeck coefficient, κ_{total} is total thermal conductivity ($\kappa_{total} = \kappa_{lat}$, lattice thermal conductivity, $+ \kappa_{el}$, electronic thermal conductivity), and T is absolute temperature. Significant enhancement in zT has been achieved mainly through the reduction of κ_{lat}.[2] However, the lattice thermal conductivity cannot be reduced lower than that of the amorphous limit, as the phonon mean free path is limited by the interatomic distance.[3] Hence, significant enhancement in power factor (σS^2) combined with intrinsic low thermal conduction is crucial for the improvement of zT in present inorganic solids. Enhancement of the σS^2 value has been achieved mainly by improvement of the Seebeck coefficient through convergence of degenerate valleys of electronic bands,[4] introduction of resonance states in the valence/conduction bands,[5] and carrier engineering.[6] On the other hand, low thermal conductivity has been achieved through scattering of heat-carrying phonons by atomic-scale point defects,[1b,7] nanoscale endotaxial inclusions,[8] all-scale hierarchical nano-/meso-architectures,[9] and inherent lattice anharmonicity.[10]

Pristine SnTe is a well-known semiconductor with huge p-type carrier density ($\sim 10^{21}$ cm^{-3}) ensuing from inherent Sn vacancies.[11] This gives rise to small Seebeck coefficient and large electrical conductivity in SnTe. SnTe exhibits crystal and electronic structures that are similar to those of PbTe.[5b,12] In SnTe, the difference in energy between the upper light-hole valence band at the L point and the lower heavy-hole valence band at the Σ point is $\sim 0.3-0.4$ eV at room temperature, which is significantly higher compared to that of PbTe (~ 0.17 eV),[11a,12] leading to negligible involvement of the heavy-hole valence band in thermoelectric transport of SnTe.[13] However, SnTe appears to be a promising high-temperature thermoelectric material based on recent reports.[14−20]

PbTe has risen to the peak of thermoelectrics via utilization of the concepts of electronic structure engineering (i.e., formation of resonance levels[5a] and valence band valley convergence[4a,9d]) and nano-/microstructure manipulation in all scales.[9a,d] Recently, these strategies have been applied to SnTe with the goal of improvement in zT relative to that of PbTe.[7,14] Additionally, iodine doping in SnTe efficiently tunes the carrier density in the light-hole valence band, which results in enhanced thermoelectric properties.[15] A noteworthy

reduction of κ_{lat} has been reported in SnTe-AgBiTe$_2$ via heat-carrying phonon scattering by point defects and Ag-rich nanostructures.[16a] Recently, thermal conductivity of SnTe has been lowered to its theoretical minimum value by introduction of matrix-encapsulated layered intergrowth nanodomains of Sn$_m$Sb$_{2n}$Te$_{3n+m}$.[16b]

Doping of Cd, Mg, Hg, Mn, and Ca in SnTe provides efficient valence band convergence, which gives rise to a significant improvement of the Seebeck coefficient of SnTe.[14,17] Introduction of indium in SnTe creates resonance states in the valence band.[5b,7,18] Although the formation of a resonance state significantly enhances the Seebeck coefficient of SnTe at room temperature, the increase in its Seebeck coefficient at high temperature is not extraordinary.[19]

Recently, we have shown that Ag doping in SnTe widens the principal band gap of SnTe, which provides significant valence band convergence and minimization of the number of the minority carriers at elevated temperature (less bipolar conduction).[20] Moreover, Ag-doped SnTe is known to show improved thermoelectric performance due to optimization of p-type carrier concentration.[21] Hence, In and Ag have distinct but complementary roles, and co-doping of Ag and In in SnTe may results in synergistic enhancement in Seebeck coefficient and power factor. The coexistence of resonance states (due to In doping) and valence band convergence (due to Cd doping) has been proven to be powerful for improving the thermoelectric efficiency of SnTe.[19] Understanding developed in these works has inspired us to study the thermoelectric properties of SnTe-AgInTe$_2$.

Here, we demonstrate the synergistic effect of In and Ag on the electronic structure and thermoelectric properties of SnTe-AgInTe$_2$ (i.e., SnAg$_x$In$_x$Te$_{1+2x}$) ingots, where In doping creates resonance level and valence band convergence is enabled by Ag doping in p-type SnTe. The electronic structure determined by first-principles density functional theoretical (DFT) shows the simultaneous formation of a resonance level and valence band convergence in SnAg$_x$In$_x$Te$_{1+2x}$, which indeed supports the experimental thermoelectric data. We have achieved a synergistic enhancement of Seebeck coefficient in SnAg$_x$In$_x$Te$_{1+2x}$ over a broad temperature range (300−860 K) compared to that of controlled In-doped SnTe and Ag-doped SnTe. Moreover, co-doping with In and Ag significantly tunes the electronic transport properties of SnTe, leading to a power factor of $\sigma S^2 \approx 31.4$ μW/cm·K^2, which is the highest among those obtained for SnTe-based materials so far. As a consequence, we have achieved maximum $zT \approx 1$ at 856 K for In and Ag co-doped SnTe, which is significantly higher than those of the controlled ingots of In-doped SnTe and Ag-doped SnTe.

■ METHODS

Chemicals. The following chemicals were used for synthesis without purification: Sn shots (99.99+%, Alfa), Te lump (99.999+%, Alfa), Ag shots (99.999%, metal basis, Alfa), and In shots (99.99+%, Alfa).

Synthesis. In order to synthesize crystalline ingots (∼7 g) of SnAg$_x$In$_x$Te$_{1+2x}$ (x = 0−0.04), we weighed Sn, Te, In, and Ag according to the desired nominal composition and then put them inside a quartz tube of 8 mm inner diameter. The tubes were evacuated under vacuum (10^{-5} Torr) and sealed by flame. The sealed tubes were then put inside a programmable box furnace. The tubes were slowly heated to 900 °C in 10 h and kept at that temperature for 10 h. The tubes were finally slowly cooled to room temperature over 12 h. Typically to synthesize SnAg$_{0.025}$In$_{0.025}$Te$_{1.05}$, Sn (3.2176 g,

27.105 mmol), Ag (73.1 mg, 0.678 mmol), In (77.8 mg, 0.678 mmol), and Te (3.6315 g, 28.46 mmol) were used.

Powder X-ray Diffraction (PXRD). We measured the PXRD of all the samples by using a Bruker D8 diffractometer with Cu Kα (λ = 1.5406 Å) radiation.

Electrical Transport. To measure σ and S, we cut and polished the ingot sample to a parallelepiped shape with dimensions of ∼2 × 2 × 8 mm^3. The temperature-dependent (300−860 K) measurement of electrical conductivity and Seebeck coefficient was carried out simultaneously under He gas by using an ULVAC-RIKO ZEM-3 machine. Electronic transport and thermal conductivity were measured in similar directions along the ingot. We checked the reversibility of the heating and cooling cycles' electrical transport data for all the samples (see a typical example in Figure S1 in the Supporting Information (SI)).

Hall Measurement. At room temperature, we determined the carrier densities (n_H) by measuring Hall coefficients (R_H) with equipment developed by Excel Instruments. We used four-contact Hall-bar geometry and a varying magnetic field up to 0.57 T during the measurements. n_H values were calculated by using the formula $n_H = 1/eR_H$, where e is the charge of an electron.

Thermal Conductivity. To measure the thermal diffusivity (D), we cut and polished the ingot to a coin-shaped sample (∼8 mm diameter and ∼2 mm thickness). Temperature-dependent (300−873 K) D values for all the samples were directly measured by using a Netzsch LFA-457 instrument, which uses a laser flash diffusivity technique. The D vs T data for all samples are given in Figure S2, SI. Heat capacity (C_p) values in the 300−873 K range were indirectly derived using a standard sample (pyroceram 9606) during the diffusivity measurement (see Figure S2, SI). We calculated total thermal conductivity as $\kappa_{total} = DC_p\rho$, where ρ is the density of the sample. We measured the ρ values of all the samples from the sample dimensions and mass, which gave ∼97% of the theoretical density (Table S1, SI).

Computational Details. We determined the electronic structures of Ag and In co-doped SnTe, controlled Ag-doped SnTe, controlled In-doped SnTe, and undoped SnTe within DFT using the Quantum Espresso package.[22] Since the atoms in these compounds have fairly high atomic numbers and masses, the relativistic effects cannot be neglected, and we included the effects of spin−orbit coupling to elucidate realistic electronic structures. Fully relativistic ultra-soft pseudopotentials and a Generalized Gradient Approximated (GGA) exchange-correlation energy with parametrized functional of Perdew, Burke, and Erzenhoff (PBE) were used.[23] Valence and semicore electronic states of Sn, Te, Ag, and In (in 4d^{10} 5s^2 5p^2, 4d^{10} 5s^2 5p^4, 4d^{10} 5s^1, and 4d^{10} 5s^2 5p^1 configurations, respectively) were treated in valence through use of these pseudopotentials. SnTe is known to crystallize in the rocksalt structure with two atoms per unit cell and $Fm\bar{3}m$ space group. Ag and In co-doped SnTe, controlled Ag-doped SnTe, controlled In-doped SnTe, and undoped SnTe were simulated with a tetragonal ($\sqrt{2}\times\sqrt{2}\times2$) supercell containing 32 atoms. Ag was substituted for Sn in the zinc blende site of SnTe, and In was substituted for Sn in the rocksalt site of SnTe in the supercell. We considered the defect pairs in the fourth-nearest-neighbor positions in the Sn sublattice for the In and Ag co-doped SnTe. Kohn−Sham wave functions and charge density were represented with a plane wave basis truncated with energy cutoffs of 50 and 400 Ry, respectively. A 14×14×10 mesh of k points was used in sampling Brillouin zone integrations (such fine mesh is necessary because many states near the gap or E_F have nontrivial dispersion). The discontinuity in occupation numbers of electronic states was smeared using a Gaussian function with a width (k_BT) of 0.003 Ry. Electronic spectra were determined at Bloch vectors along high-symmetry lines (Γ - X - M - Γ - Z - R - A - Z) in the Brillouin zone.

■ RESULTS AND DISCUSSION

The crystalline ingots of SnTe and SnAg$_x$In$_x$Te$_{1+2x}$ (x = 0.01−0.04) were synthesized via solid-state melting reaction at 900 °C followed by slow cooling. Figure 1a shows the PXRD
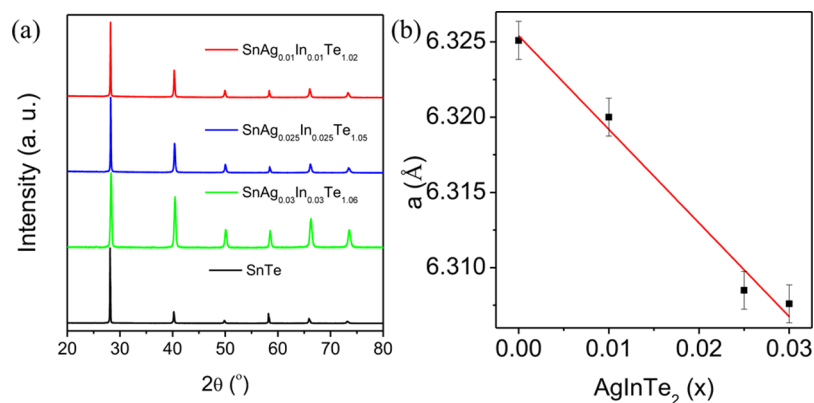
Figure 1. (a) Powder XRD patterns of $SnAg_xIn_xTe_{1+2x}$ (x = 0−0.03) samples. (b) Lattice parameters (a) of $SnAg_xIn_xTe_{1+2x}$ vs $AgInTe_2$ concentration (x); solid line indicates the solid solution behavior.
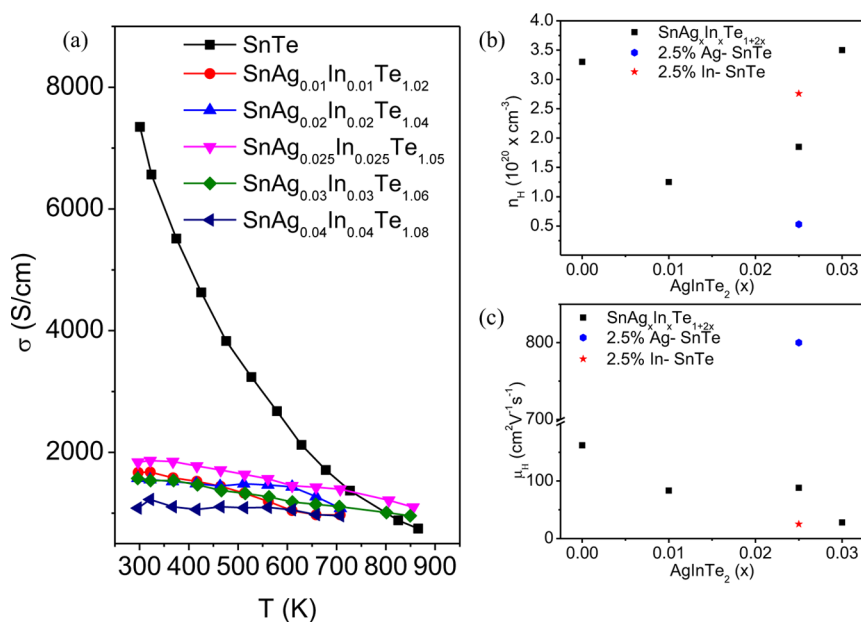
Figure 2. (a) Temperature-dependent electrical conductivity (σ) of $SnAg_xIn_xTe_{1+2x}$ (x = 0−0.04) samples. (b) Carrier concentration (n_H) and (c) carrier mobility (μ_H) at room temperature with respect to the $AgInTe_2$ concentration (x) in $SnAg_xIn_xTe_{1+2x}$.

pattern of $SnAg_xIn_xTe_{1+2x}$ (x = 0.01−0.04), where all Bragg's diffraction peaks can be indexed on the basis of the cubic SnTe, with $Fm\bar{3}m$ space group. The lattice parameters of $SnAg_xIn_xTe_{1+2x}$ decrease with increasing $AgInTe_2$ content, which is consistent with the difference in lattice parameters between SnTe (6.3251 Å) and $AgInTe_2$ (6.02 Å) (Figure 1b). A linear decrease in the lattice parameter with increased concentration of $AgInTe_2$ and higher angle shift of PXRD peak confirms the solid solution nature of $SnAg_xIn_xTe_{1+2x}$ samples.

In Figure 2a, we present electrical conductivity (σ) of $SnAg_xIn_xTe_{1+2x}$ (x = 0.0−0.04) in the 300−860 K range. Electrical conductivity steadily decreases with increasing temperature, confirming degenerate semiconducting behavior of all the $SnAg_xIn_xTe_{1+2x}$ samples. The room-temperature electrical conductivity decreases with increasing $AgInTe_2$ concentration, which can be attributed to reduced carrier mobility of the samples. Typically, the room-temperature value for $SnAg_{0.01}In_{0.01}Te_{1.02}$ is $\sigma \approx 1668$ S/cm, which decreases to 957 S/cm at 707 K. To estimate the carrier type and concentration, room-temperature Hall measurements were carried out for all $SnAg_xIn_xTe_{1+2x}$ samples. Hole conduction

(p-type) in $SnAg_xIn_xTe_{1+2x}$ was confirmed by the positive values of R_H. The resultant carrier concentration n_H and mobility μ_H are plotted in Figure 2b,c. Hole concentration shows an interesting trend with increasing $AgInTe_2$ concentration: it drops below the intrinsic value at the beginning and starts to increase when x > 0.01. For small concentration of $AgInTe_2$, Ag and In mainly occupy Sn vacancies.[5b,19,21] SnTe is a typical nonstoichiometric compound with inherent Sn vacancies.[13] Thus, the co-doping of In and Ag in SnTe reduces the Sn vacancies when the concentrations of co-dopants are small. As the doping level is increased, however, once all the Sn vacancies are filled, the remaining In/Ag substitute for Sn, and the p-type carrier density increases. Similar behaviors have been observed in SnTe-based systems, where In or Ag atoms first act as donor dopant followed by its p-type nature.[5b,21] Controlled 2.5 mol% In-doped SnTe sample does not change the p-type carrier concentration in SnTe, but higher concentrations of In doping in SnTe are known to increase the p-type carrier concentration.[5b] Controlled 2.5 mol% Ag-doped SnTe sample exhibits lower p-type carrier concentration compared to SnTe due to reduction of Sn vacancies by Ag doping, but higher

concentrations of Ag doping increase the p-type carrier concentration.[20]

Carrier mobility, defined as $\mu_H = \sigma/n_H e$, at room temperature is plotted as a function of dopant concentration in Figure 2c. Pristine SnTe has a hole mobility of ~160 cm^2 V^{-1} s^{-1} at 300 K, which together with its high hole density produces a large electrical conductivity of ~7350 S/cm at room temperature. Upon co-doping of In and Ag, carrier mobility decreases significantly due to solid solution point defect scattering and possibly due to impurity scattering caused by In doping,[5b,20] which together lead to the decline in electrical conductivity described above. However, controlled Ag doping increases the carrier mobility in SnTe (Figure 2c). Thus, the contrasting but beneficial effects of In and Ag are indeed important in overall enhancement of the thermoelectric performance of SnTe.

The weaker temperature dependence of the electrical conductivity of $SnAg_xIn_xTe_{1+2x}$ can be attributed to reduced carrier−phonon scattering, which results in higher σ at $T > 750$ K compared to that of the pristine SnTe (Figure 2a).[18] In order to understand the effects of Ag and In, transport properties of controlled Ag-doped SnTe and In-doped SnTe were analyzed separately (Figure S3, SI). The 2.5 mol% In-doped SnTe sample has a lower conductivity as compared to 2.5 mol% Ag-doped SnTe due to lower carrier mobility in the In-doped sample compared to that in Ag-doped SnTe. In and Ag co-doped samples have an intermediate value of conductivity, which can be attributed to intermediate carrier concentration and mobility of $SnAg_xIn_xTe_{1+2x}$ samples.

Temperature dependences of Seebeck coefficients for $SnAg_xIn_xTe_{1+2x}$, controlled 2.5 mol% In-doped SnTe, and controlled 2.5 mol% Ag-doped SnTe are shown in Figure 3 and Figure S3, SI. All the samples exhibit positive Seebeck coefficients, which are in good agreement with the positive values of Hall coefficients. For all the samples, Seebeck coefficient increases with increasing temperature. Interestingly, for $SnAg_xIn_xTe_{1+2x}$, the Seebeck coefficients dramatically increased relative to those of the controlled In- or Ag-doped SnTe over the whole temperature range (Figure S3, SI). Typically, for $SnAg_{0.025}In_{0.025}Te_{1.05}$, the room-temperature Seebeck coefficient is ~97 μV/K, which increases linearly to 167 μV/K at 856 K. This confirms the synergistic effect of Ag and In on the thermoelectric properties of SnTe, leading to significant enhancement of the Seebeck coefficient of SnTe over a broad temperature range.

To understand the origin of the enhanced Seebeck coefficient, we compared the room-temperature S as a function of n_H with the well-established Pisarenko line of SnTe, which was calculated on the basis of a two-valence-band model by Ren and co-workers (Figure 3b).[5b] This model considers the energy difference between light-hole valence band (effective mass ~0.168m_e) and heavy-hole valence band (effective mass of ~1.92m_e) to be 0.35 eV for SnTe.[5b] The Seebeck coefficient of pristine SnTe falls exactly on the Pisarenko line, demonstrating the strength of the adopted physical model.[11a] Controlled In-doped SnTe samples show a relatively higher S value as compared to the Pisarenko plot, which is attributed to resonance level formation in the valence band of SnTe introduced by the In dopant.[5b,7] This resulted in a lower value of hole mobility via a sharp enhancement in effective mass and carrier scattering (Figure 2c). Although the reduced hole concentration is expected to decrease the contribution of the heavy-hole valence band to the Seebeck coefficient in controlled Ag-doped SnTe, Ag-doped samples also show
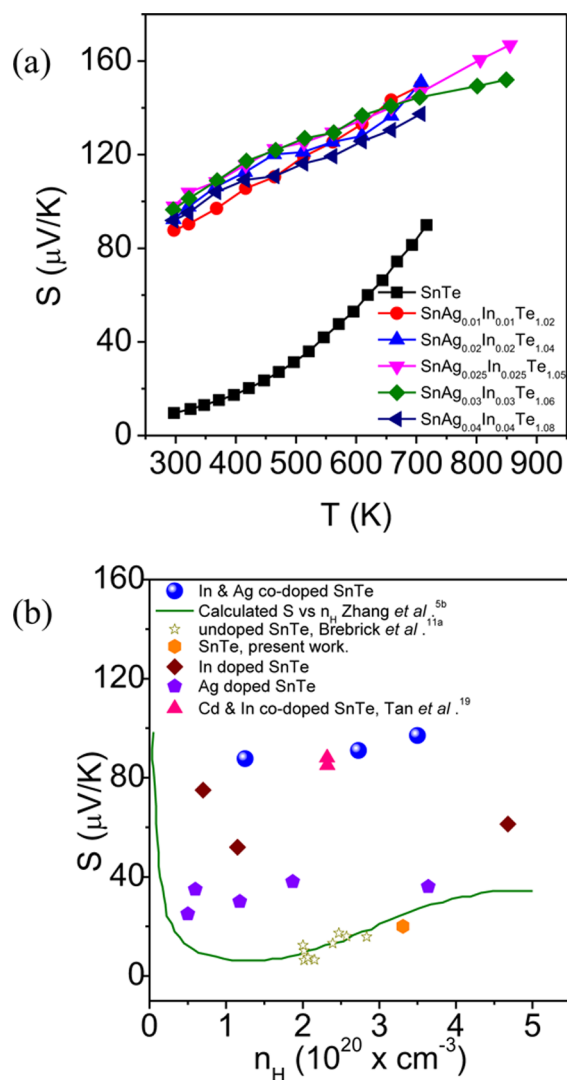
Figure 3. (a) Temperature-dependent Seebeck coefficient (S) of $SnAg_xIn_xTe_{1+2x}$ samples. (b) Room-temperature S vs n_H plot of the present $SnAg_xIn_xTe_{1+2x}$ samples. The solid line is a Pisarenko plot calculated using a two-valence-band model.[5b] For comparison, S vs n_H experimental data of undoped SnTe,[11a] controlled Ag-doped SnTe (present work), controlled In-doped SnTe (present work), and In and Cd co-doped SnTe[19] are also given in (b).

relatively higher Seebeck coefficients as compared to the theoretical Pisarenko curve (Figure 3b). The Seebeck coefficient values of Ag-doped samples are comparable to previously reported S values of Cd/Mg-doped SnTe, where enhancement of S was attributed to the valence band convergence.[14] Interestingly, we have resolved the band gap (E_g) of the Ag-doped SnTe by diffuse infrared (IR) reflectance spectroscopy (Figure S4, SI). Ag doping increases the band gap of SnTe, suggesting that effective valence band convergence is achieved, which was also indicated in our previous study.[20] The higher value of the Seebeck coefficient and large band gap motivated us to investigate the electronic structure of a Ag-doped SnTe sample (see discussion below). $SnAg_xIn_xTe_{1+2x}$ samples exhibit much higher Seebeck coefficients as compared to those of the controlled Ag-doped SnTe and In-doped SnTe samples with similar carrier concentrations (Figure 3b). This indicates that resonance level introduced by the In and band convergence caused by the Ag synergistically enhance the
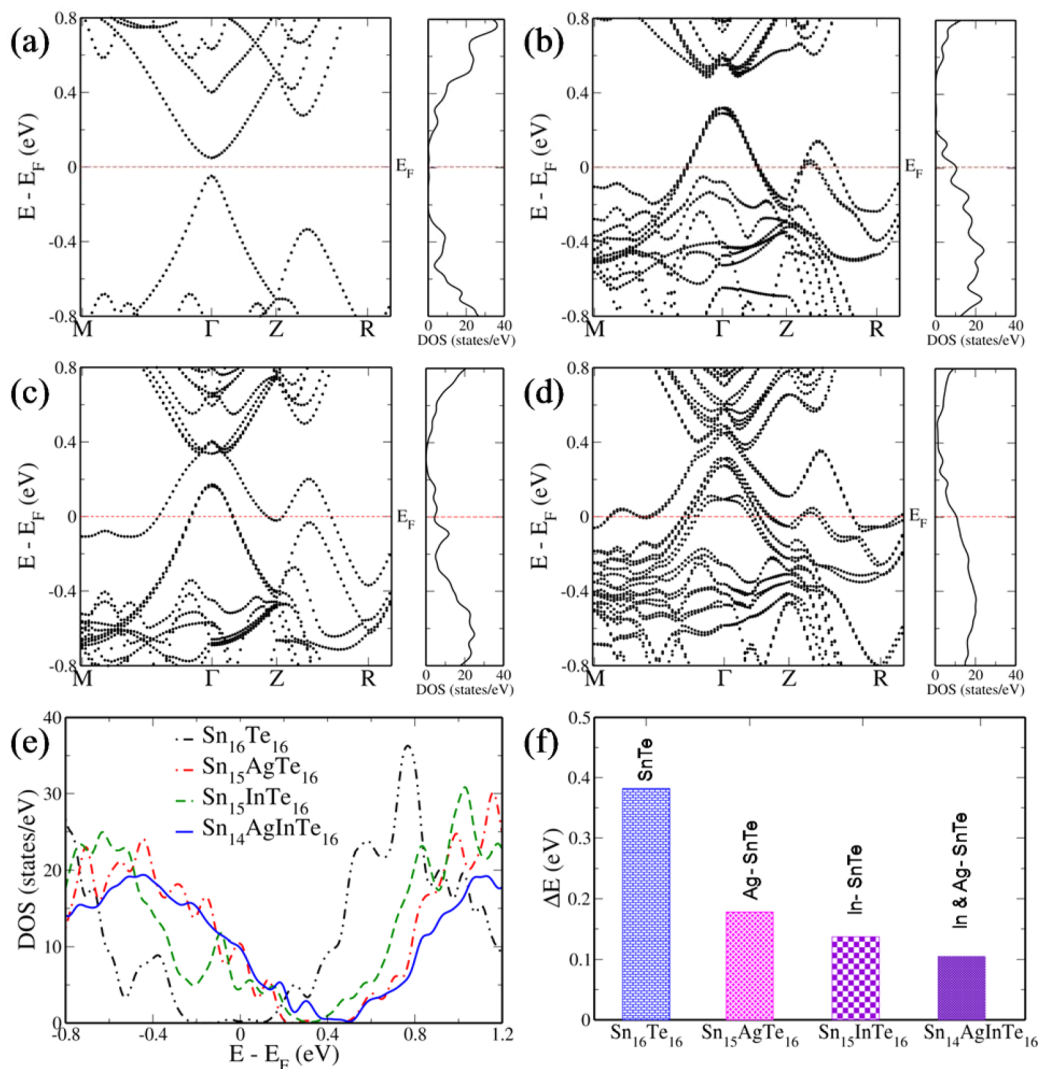
Figure 4. Electronic structure and density of states of (a) $Sn_{16}Te_{16}$, (b) $Sn_{15}AgTe_{16}$, (c) $Sn_{15}InTe_{16}$, and (d) $Sn_{14}AgInTe_{16}$ supercells as a function of wave vector in the supercell Brillouin zone. The energies are shifted with respect to the Fermi energy, which is set to zero. The band gap appears at the Γ point and heavy-hole band at $Z + \delta$ in the $\sqrt{2} \times \sqrt{2} \times 2$ tetragonal supercell. The VBM and CBM occurring at the L point in the rocksalt cell of SnTe fold onto the Γ point, and the heavy-hole valence band appearing along Σ folds onto $Z + \delta$ in the case of the present 32-atom $\sqrt{2} \times \sqrt{2} \times 2$ tetragonal supercell. (e) DOS near the top of the valence band. (f) Energy separations, ΔE, between the upper valence band at the Γ point and the lower valence band at the $Z + \delta$ point for pristine SnTe, In- and Ag-doped SnTe, and In and Ag co-doped SnTe.

Seebeck coefficient further in $SnAg_xIn_xTe_{1+2x}$. We have compared the room-temperature Seebeck coefficient of $SnAg_xIn_xTe_{1+2x}$ samples with those previously reported for In and Cd co-doped SnTe.[19] Similar S vs n_H behavior compared to that of In and Cd co-doped SnTe and a remarkably higher value of Seebeck coefficient compared to those of controlled Ag-doped SnTe and In-doped SnTe motivated us to investigate the effects of In and Ag on the electronic structure of the SnTe system.

To understand the origin of enhancement in Seebeck coefficient of SnTe upon co-doping with Ag and In, we used DFT calculations to determine the electronic structure of Ag and In co-doped SnTe, controlled Ag-doped SnTe, controlled In-doped SnTe, and undoped SnTe (Figure 4). Bloch wave functions of a supercell are related to those of a single unit cell according to a Brillouin zone folding based on the periodicity of reciprocal space. For the $\sqrt{2} \times \sqrt{2} \times 2$ supercell used in these simulations, the principal valence band (light-hole) maximum (VBM) and conduction band minimum (CBM) occur at the Γ

point, and the heavy-hole valence band occurs at $Z + \delta$ along the $Z \rightarrow R$ direction. The VBM and CBM occur at the L point in the Brillouin zone of a single cell of cubic SnTe. In the Brillouin zone of the supercell considered here, they fold back to the Γ point (zone center). Similarly, the heavy-hole valence band along the Σ line corresponds to the states at $Z + \delta$ in the Brillouin zone of the 32-atom $\sqrt{2} \times \sqrt{2} \times 2$ tetragonal supercell. We find that the band gap of SnTe increases with Ag doping, consistent with the trend in the experimental band gaps measured with diffuse reflectance spectroscopy (Figure S4, SI). Our estimated band gap for SnTe was ~0.097 eV when the spin−orbit coupling was included (in comparison to the estimate of ~0.049 eV obtained from calculations without spin−orbit coupling). The band gap of $Sn_{16}Te_{16}$ at the Γ point increases to ~0.230 eV with doping of 6.25 mol% Ag for Sn atoms (Figure 4b). A significant decrease in the separation between the energies of the light- and heavy-hole valence bands of SnTe is achieved with Ag doping, from ~0.382 eV in pristine SnTe to ~0.178 eV in the 6.25 mol% Ag-doped SnTe (Figure
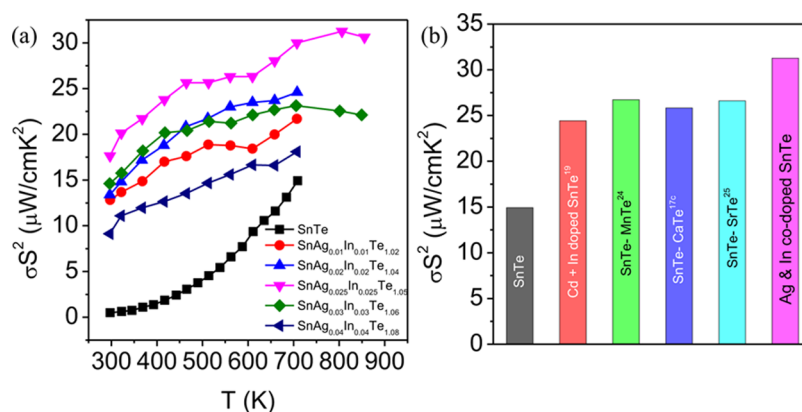
Figure 5. Temperature-dependent power factors (σS^2) of SnAg$_x$In$_x$Te$_{1+2x}$ samples. (b) Comparison of the high-temperature power factor of the present SnAg$_x$In$_x$Te$_{1+2x}$ sample with those of the previously reported high-performance In and Cd co-doped SnTe,[19] SnTe-MnTe,[24] SnTe-CaTe,[17c] and SnTe-SrTe.[25]

4f). Thus, incorporation of Ag in SnTe leads to an increase in the valence band degeneracy, and such valence band convergence is expected to result in enhancement of the Seebeck coefficient as the two bands contribute to the asymmetry reflected in the slope of the density of states (DOS) at or near the Fermi energy.[14a] Similar modifications have been found in the bands of Mg-, Cd-, Cd/Hg-, and Cd/In-doped SnTe.[14,17a,19] For 6.25 mol% In-doped SnTe, the calculated DOS reveals well-defined peaks within the valence band near the Fermi level, indicating a resonance level (Figure 4c,e). In this case, too, we see that there is some degree of convergence of light- and heavy-hole valence bands. The energy separation between the two valence bands decreases to ∼0.137 eV (Figure 4f), in agreement with the reported value of 0.2 eV for ∼4% In-doped SnTe.[19] The electronic structure of Ag and In co-doped SnTe reveals both the formation of resonance state and the convergence of the valence bands (Figure 4d,e). The energy difference between the light- and heavy-hole valence bands further reduces to ∼0.105 eV (Figure 4f), showing the synergistic effects of Ag and In (Figure 4). Therefore, coexisting resonance level and valence band convergence in Ag and In co-doped SnTe are responsible for the observed remarkable enhancement in the Seebeck coefficient.

The temperature-dependent power factors of SnAg$_x$In$_x$Te$_{1+2x}$ samples are presented in Figure 5. Ag and In co-doped SnTe samples show significantly high value of the σS^2 over a broad range of temperature due to the enhanced Seebeck coefficient and an optimal electrical conductivity. Figure S3c in SI compares the power factors for pristine, In- and Ag-doped, and In and Ag co-doped SnTe. Clearly, In and Ag co-doped SnTe combines the advantages of In and Ag doping. This indicates an additive and possibly synergistic effect of co-doping over individual dopant in SnTe. Typically, the room-temperature σS^2 value for SnAg$_{0.025}$In$_{0.025}$Te$_{1.05}$ is ∼18 μW/cm·K^2 which increases to ∼31.4 μW/cm·K^2 at 856 K. We have compared the power factor of SnAg$_{0.025}$In$_{0.025}$Te$_{1.05}$ with the previously reported In and Cd co-doped SnTe,[19] SnTe-MnTe,[24] SnTe-CaTe,[17c] and SnTe-SrTe[25] (Figure 5b). Maximum power factor values obtained in the present SnAg$_x$In$_x$Te$_{1+2x}$ ingot samples are higher compared to that of the previously reported SnTe-based system. While the In and Ag co-doped SnTe exhibits a Seebeck coefficient similar to that of In and Cd co-doped SnTe (Figure 3b), the carrier mobility is relatively higher in In and Ag co-doped SnTe compared to In

and Cd co-doped SnTe with similar carrier concentrations.[19] Thus, we observe higher power factor in In and Ag co-doped SnTe compared to that of In and Cd co-doped SnTe.

In Figure 6, we present the temperature-dependent κ_{total}, κ_{el}, and κ_{lat} values of SnAg$_x$In$_x$Te$_{1+2x}$ (x = 0−0.04) samples. The κ_{el} = $L\sigma T$ values were estimated from calculated Lorenz number
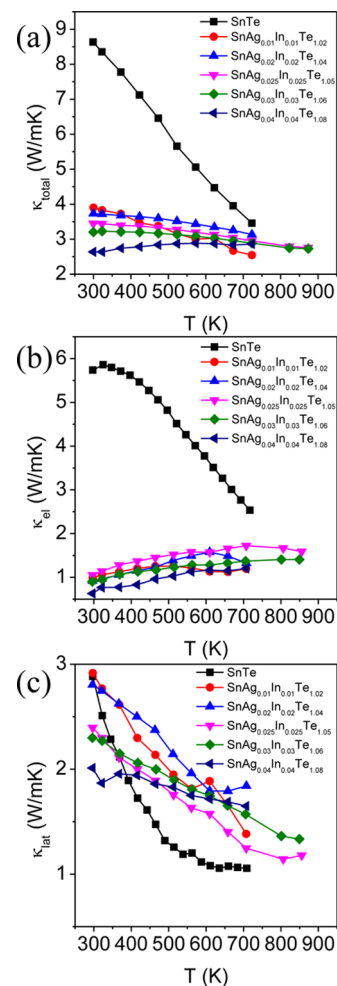

Figure 6. Temperature-dependent (a) total thermal conductivity (κ_{total}), (b) electronic thermal conductivity (κ_{el}), and (c) lattice thermal conductivity (κ_{lat}) of SnAg$_x$In$_x$Te$_{1+2x}$ samples.

(L), measured electrical conductivity, and absolute temperature. L values were calculated (Figure S5, SI) from reduced Fermi energy, which is obtained from the fitting of the respective temperature-dependent Seebeck data as indicated elsewhere.[9a,26] Ag and In co-doping in SnTe optimizes the temperature-dependent κ_{total} by controlling the κ_{el}. κ_{total} decreases with increasing the AgInTe$_2$ concentration due to the systematic decrease in κ_{el}. Typically, the κ_{total} value measured for SnAg$_{0.025}$In$_{0.025}$Te$_{1.05}$ is ~3.45 W m^{-1} K^{-1} at 300 K, which decreases to ~2.72 W m^{-1} K^{-1} at 873 K. The κ_{lat} was obtained after subtraction of the electronic part, κ_{el}, from κ_{total}. Typically, the room-temperature value of κ_{lat} measured for SnAg$_{0.025}$In$_{0.025}$Te$_{1.05}$ is ~2.39 W m^{-1} K^{-1}, which decreases to ~1.17 W m^{-1} K^{-1} at 876 K. Although we have not observed any systematic trend for κ_{lat} with varying doping concentration in SnTe, κ_{lat} values of In and Ag co-doped SnTe are slightly higher compared to those of undoped SnTe. In principle, increased point defects in the SnTe sample are expected to lower the κ_{lat} value. The above result indicates that the Lorenz number value used cannot properly account for the electronic contribution to thermal conductivity. It was shown earlier that, in degenerate semiconductors with multiple bands coexistent at the Fermi level, a complex inter-valley scattering can occur in which the carriers move from one valley to the other, transferring larger amounts of heat than what is predicted by the degenerate L value.[27] Such an inter-valley carrier scattering has been evidenced in Na and K co-doped PbTe samples whose calculated κ_{lat} values were relatively higher compared to those of undoped PbTe due to an underestimation of κ_{el}.[28] In and Ag co-doping in SnTe increases the valence band convergence and the hole concentration, which possibly facilitates the inter-valley carrier scattering.

In Figure 7, we present temperature-dependent zT of SnAg$_x$In$_x$Te$_{1+2x}$ (x = 0–0.04) samples. Combined effect of In
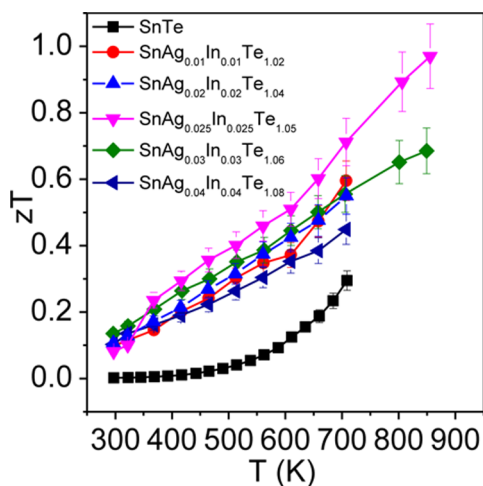
Figure 7. Temperature dependence of thermoelectric figure of merit (zT) of SnAg$_x$In$_x$Te$_{1+2x}$ samples with 10% error bar.

and Ag enhances the zT significantly. The highest zT was measured to be ~1.0 at 856 K for SnAg$_{0.025}$In$_{0.025}$Te$_{1.05}$, which is considerably higher than that of the undoped SnTe, controlled In-doped SnTe and Ag-doped SnTe. Average zT of SnAg$_{0.025}$In$_{0.025}$Te$_{1.05}$ is ~0.6 by considering the hot and cold ends to be 860 and 300 K, respectively, which is comparable to the other high-performance SnTe-based materials.

CONCLUSIONS

SnTe-AgInTe$_2$ (SnAg$_x$In$_x$Te$_{1+2x}$) shows an enhanced thermoelectric performance over a broad temperature range due to the synergistic effect of resonance level formation and the convergence of valence bands. Indium doping creates a resonance state in the valence band of SnTe. Ag doping increases the principal band gap of SnTe, resulting in a decrease of the energy separation between two valence bands (light- and heavy-holes valence bands) of SnTe and consequent suppression of the bipolar conduction at high temperature. Effective convergence of the valence bands and the presence of a resonance level near the Fermi energy synergistically enhance the Seebeck coefficient in Ag and In co-doped SnTe, resulting in a remarkable increase in power factor to 31.4 μW/cm·K^2, which is the highest power factor of SnTe-based compounds reported so far. As a result, the highest $zT \approx 1$ at 856 K has been achieved. Hence, SnAg$_x$In$_x$Te$_{1+2x}$ shows the collective advantage of Ag and In doping on the overall thermoelectric performance of SnTe. The improved zT values over the broad range 300–860 K found in the In and Ag co-doped SnTe make it a useful thermoelectric material that deserves further investigation and performance optimization through minimization of its lattice thermal conductivity.

ASSOCIATED CONTENT

Ⓢ Supporting Information

The Supporting Information is available free of charge on the ACS Publications website at DOI: 10.1021/jacs.6b08382.

> Thermoelectric properties measured in heating–cooling cycle; thermal diffusivity, and C$_p$; thermoelectric properties of controlled undoped and singly doped SnTe samples; electronic absorption spectra of Ag-doped SnTe and Lorenz number L; densities of all samples (PDF)

AUTHOR INFORMATION

Corresponding Author

*kanishka@jncasr.ac.in

Notes

The authors declare no competing financial interest.

ACKNOWLEDGMENTS

REFERENCES

(1) (a) Sootsman, J. R.; Chung, D. Y.; Kanatzidis, M. G. *Angew. Chem., Int. Ed.* **2009**, *48*, 8616–8639. (b) Zhao, L.-D.; Dravid, V. P.; Kanatzidis, M. G. *Energy Environ. Sci.* **2014**, *7*, 251–268. (c) Kim, H. S.; Liu, W.; Chen, G.; Chu, C.-W.; Ren, Z. *Proc. Natl. Acad. Sci. U. S. A.* **2015**, *112*, 8205–8210.

(2) Hsu, K. F.; Loo, S.; Guo, F.; Chen, W.; Dyck, J. S.; Uher, C.; Hogan, T.; Polychroniadis, E. K.; Kanatzidis, M. G. *Science* **2004**, *303*, 818–821.

(3) Slack, G. A. *Solid State Phys.* **1979**, *34*, 1–71.

(4) (a) Pei, Y.; Shi, X.; LaLonde, A.; Wang, H.; Chen, L.; Snyder, G. J. *Nature* **2011**, *473*, 66–69. (b) Zhao, L.; Wu, H.; Hao, S.; Wu, C.-I.; Zhou, X.; Biswas, K.; He, J.; Hogan, T. P.; Uher, C.; Wolverton, C.; et al. *Energy Environ. Sci.* **2013**, *6*, 3346–3355.

(5) (a) Heremans, J. P.; Jovovic, V.; Toberer, E. S.; Saramat, A.; Kurosaki, K.; Charoenphakdee, A.; Yamanaka, S.; Snyder, G. J. *Science*

2008, *321*, 554−557. (b) Zhang, Q.; Liao, B.; Lan, Y.; Lukas, K.; Liu, W.; Esfarjani, K.; Opeil, C.; Broido, D.; Chen, G.; Ren, Z. *Proc. Natl. Acad. Sci. U. S. A.* **2013**, *110*, 13261−13266.

(6) (a) Guin, S. N.; Srihari, V.; Biswas, K. *J. Mater. Chem. A* **2015**, *3*, 648−655. (b) Guin, S. N.; Chatterjee, A.; Negi, D. S.; Datta, R.; Biswas, K. *Energy Environ. Sci.* **2013**, *6*, 2603−2608.

(7) Banik, A.; Biswas, K. *J. Mater. Chem. A* **2014**, *2*, 9620−9625.

(8) Biswas, K.; He, J.; Zhang, Q.; Wang, G.; Uher, C.; Dravid, V. P.; Kanatzidis, M. G. *Nat. Chem.* **2011**, *3*, 160−166.

(9) (a) Biswas, K.; He, J.; Blum, I. D.; Wu, C.-I.; Hogan, T. P.; Seidman, D. N.; Dravid, V. P.; Kanatzidis, M. G. *Nature* **2012**, *489*, 414−418. (b) Zhao, L.-D.; Hao, S.; Lo, S.-H.; Wu, C.-I.; Zhou, X.; Lee, Y.; Li, H.; Biswas, K.; Hogan, T. P.; Uher, C.; Wolverton, C.; Dravid, V. P.; Kanatzidis, M. G. *J. Am. Chem. Soc.* **2013**, *135*, 7364−7370. (c) Poudel, B.; Hao, Q.; Ma, Y.; Lan, Y.; Minnich, A.; Yu, B.; Yan, X.; Wang, D.; Muto, A.; Vashaee, D.; Chen, X.; Liu, J.; Dresselhaus, M. S.; Chen, G.; Ren, Z. *Science* **2008**, *320*, 634−638. (d) Tan, G.; Shi, F.; Hao, S.; Zhao, L.-D.; Chi, H.; Zhang, X.; Uher, C.; Wolverton, C.; Dravid, V. P.; Kanatzidis, M. G. *Nat. Commun.* **2016**, *7*, 12167.

(10) (a) Zhao, L.-D.; Tan, G.; Hao, S.; He, J.; Pei, Y.; Chi, H.; Wang, H.; Gong, S.; Xu, H.; Dravid, V. P.; Uher, C.; Snyder, G. J.; Wolverton, C.; Kanatzidis, M. G. *Science* **2016**, *351*, 141−144. (b) Morelli, D. T.; Jovovic, V.; Heremans, J. P. *Phys. Rev. Lett.* **2008**, *101*, 035901. (c) Jana, M. K.; Pal, K.; Waghmare, U. V.; Biswas, K. *Angew. Chem., Int. Ed.* **2016**, *55*, 7792−7796. (d) Zhao, L.-D.; Lo, S.-H.; Zhang, Y.; Sun, H.; Tan, G.; Uher, C.; Wolverton, C.; Dravid, V. P.; Kanatzidis, M. G. *Nature* **2014**, *508*, 373−377.

(11) (a) Brebrick, R.; Strauss, A. *Phys. Rev.* **1963**, *131*, 104. (b) Rogacheva, E. I. *J. Phys. Chem. Solids* **2008**, *69*, 259−268.

(12) Rogers, L. M. *J. Phys. D: Appl. Phys.* **1968**, *1*, 845.

(13) Brebrick, R. *J. Phys. Chem. Solids* **1963**, *24*, 27−36.

(14) (a) Banik, A.; Shenoy, U. S.; Anand, S.; Waghmare, U. V.; Biswas, K. *Chem. Mater.* **2015**, *27*, 581−587. (b) Tan, G.; Zhao, L.-D.; Shi, F.; Doak, J. W.; Lo, S.-H.; Sun, H.; Wolverton, C.; Dravid, V. P.; Uher, C.; Kanatzidis, M. G. *J. Am. Chem. Soc.* **2014**, *136*, 7006−7017.

(15) Zhou, M.; Gibbs, Z. M.; Wang, H.; Han, Y.; Xin, C.; Li, L.; Snyder, G. J. *Phys. Chem. Chem. Phys.* **2014**, *16*, 20741−20748.

(16) (a) Tan, G.; Shi, F.; Sun, H.; Zhao, L.-D.; Uher, C.; Dravid, V. P.; Kanatzidis, M. G. *J. Mater. Chem. A* **2014**, *2*, 20849−20854. (b) Banik, A.; Vishal, B.; Perumal, S.; Datta, R.; Biswas, K. *Energy Environ. Sci.* **2016**, *9*, 2011−2019.

(17) (a) Tan, G.; Shi, F.; Doak, J. W.; Sun, H.; Zhao, L.-D.; Wang, P.; Uher, C.; Wolverton, C.; Dravid, V. P.; Kanatzidis, M. G. *Energy Environ. Sci.* **2015**, *8*, 267−277. (b) Tan, G.; Shi, F.; Hao, S.; Chi, H.; Bailey, T. P.; Zhao, L.-D.; Uher, C.; Wolverton, C.; Dravid, V. P.; Kanatzidis, M. G. *J. Am. Chem. Soc.* **2015**, *137*, 11507−11516. (c) Al Rahal Al Orabi, R.; Mecholsky, N. A.; Hwang, J.; Kim, W.; Rhyee, J.-S.; Wee, D.; Fornari, M. *Chem. Mater.* **2016**, *28*, 376−384.

(18) Tan, G.; Zeier, W. G.; Shi, F.; Wang, P.; Snyder, G. J.; Dravid, V. P.; Kanatzidis, M. G. *Chem. Mater.* **2015**, *27*, 7801−7811.

(19) Tan, G.; Shi, F.; Hao, S.; Chi, H.; Zhao, L.-D.; Uher, C.; Wolverton, C.; Dravid, V. P.; Kanatzidis, M. G. *J. Am. Chem. Soc.* **2015**, *137*, 5100−5112.

(20) Banik, A.; Biswas, K. *J. Solid State Chem.* **2016**, *242*, 43.

(21) Zhang, L.; Wang, J.; Cheng, Z.; Sun, Q.; Li, Z.; Dou, S. *J. Mater. Chem. A* **2016**, *4*, 7936−7942.

(22) Giannozzi, P.; Baroni, S.; Bonini, N.; Calandra, M.; Car, R.; Cavazzoni, C.; Ceresoli, D.; Chiarotti, G. L.; Cococcioni, M.; Dabo, I.; et al. *J. Phys.: Condens. Matter* **2009**, *21*, 395502.

(23) Perdew, J. P.; Burke, K.; Ernzerhof, M. *Phys. Rev. Lett.* **1996**, *77*, 3865−3868.

(24) Wu, H.; Chang, C.; Feng, D.; Xiao, Y.; Zhang, X.; Pei, Y.; Zheng, L.; Wu, D.; Gong, S.; Chen, Y.; He, J.; Kanatzidis, M. G.; Zhao, L.-D. *Energy Environ. Sci.* **2015**, *8*, 3298−3312.

(25) Zhao, L.-D.; Zhang, X.; Wu, H.; Tan, G.; Pei, Y.; Xiao, Y.; Chang, C.; Wu, D.; Chi, H.; Zheng, L.; Gong, S.; Uher, C.; He, J.; Kanatzidis, M. G. *J. Am. Chem. Soc.* **2016**, *138*, 2366−2373.

(26) Zhao, L.-D.; Lo, S.-H.; He, J.; Li, H.; Biswas, K.; Androulakis, J.; Wu, C.-I.; Hogan, T. P.; Chung, D.-Y.; Dravid, V. P.; Kanatzidis, M. G. *J. Am. Chem. Soc.* **2011**, *133*, 20476−20487.

(27) Kolomoets, N. V. *Sov. Phys. Solid State* **1966**, *8*, 799.

(28) Androulakis, J.; Todorov, I.; Chung, D.-Y.; Ballikaya, S.; Wang, G.; Uher, C.; Kanatzidis, M. *Phys. Rev. B: Condens. Matter Mater. Phys.* **2010**, *82*, 115209.